Proceedings of the 7th International Symposium on Cavitation
CAV2009
August 17-22, 2009, Ann Arbor, Michigan, USA

CAV2009 – Paper No. 61

Cavitation Patterns on a Plano-Convex Hydrofoil in a High-Speed Cryogenic Cavitation Tunnel

Yutaka Ito
Tokyo Institute of Technology
Yokohama, Kanagawa, Japan

Tsukasa Nagayama
Toyota Motor Corporation
Toyota, Aichi, Japan

Takao Nagasaki
Tokyo Institute of Technology
Yokohama, Kanagawa, Japan

ABSTRACT

Cavitation around a plano-convex hydrofoil has been observed using a cryogenic cavitation tunnel of a blowdown type. An approximately 300mm long test section with flow visualization was set between the 100L upper and lower tanks. The working fluids were water and liquid nitrogen. Experiments with emphasis on periodical shedding of cloud cavitation were performed for three channels, 20, 30 and 60 mm in width, and two hydrofoils, 20 and 60mm in chord length L_C. Inlet velocity u_{in} and cavitation number σ were varied between 3.8 and 19.5 m/sec, and −1.83 and 19.35, respectively. Incident angle was fixed at 8º. Observed cavitation patterns are sorted according to the maximum cavitation length L_{max} compared to L_C. Type X is defined as no cavitation, type A as $0<L_{max}\leq L_C$, type B as $L_C<L_{max}\leq 2L_C$, and type C as $L_{max}>2L_C$. Type B has either the periodical shedding mode or the steady mode, so type PB is defined as type B with periodical shedding and type SB as type B under steady condition. Apparently types A and C are almost steady. Type PB solely occurs in the case that L_{max} is comparable to L_C. The cavitation patterns are mapped in the diagram of the degree of subcooling $P_{in}-P_{sat}$ versus the dynamic pressure $\rho u_{in}^2/2$ because they are not organized only by $\sigma=(P_{in}-P_{sat})/(\rho u_{in}^2/2)$. It is suggested that the maximum cavitation thickness is controlled by the similarity laws of hydrofoils for types SB and C.

INTRODUCTION

Cavitation is one of the most difficult problems to be surmounted in the development of turbo-pumps for liquid fuel rocket engines. Because high performance engines require high combustion pressure, their turbo-pumps have to operate at high rotating speed. The best performance of the pump can be obtained when cavitation occurs stably at high rotating speed, therefore it is necessary to allow controllable cavitation to form in the pump. Although conventional design methods of pumps against cavitation are available for water, current large size main engines utilize cryogens as a fuel and an oxidizer, for examples, LH_2 and LOX for U.S. RS-68, U.S. SSME, Japan's LE-7A and Europe's Valcain2, or kerosene and LOX for Russia's RD-180. Because cryogens have thermodynamic features called "thermodynamic effects" different from ordinary fluids like water, cryogenic cavitation is complicated, and it is hard to control cryogenic cavitation without deeply understanding its behavior and its influences on the pump performance. Consequently, experiments on cryogenic cavitation with visualization play a very important role in clarifying the features of cryogenic cavitation at the moment, and in getting knowledge of how to allow controllable cavitation in the near future.

Wade et al. (1966) [1] carried out a visualization study on water cavitation around a plano-convex hydrofoil, as well as measurements of lift and drag coefficients. Their photos of cavitation on the hydrofoil are very useful to recognize the cavity oscillation. Le et al. (1993) [2] noted the difference of cavitation profiles by means of flow visualization in cases of various cavitation numbers σ and angles of the incidence *AOI*. Kjeldsen et al. (1999) [3] mapped cavitation types and cavity length by combination of σ and *AOI*, and indicated the region of periodical shedding of cloud cavitation by using the Strouhal number. Franc (2001) [4] showed a relationship that gives the frequency of periodical oscillation as a function of cavitation compliance, and the length and area of the upstream duct from

the viewpoint of system instability. Callenaere (2001) [5] used a diverging step in a water tunnel to investigate the instability of a partial cavity induced by a re-entrant jet. He revealed that an adverse pressure gradient plays an important role to trigger the re-entrant jet, and the interaction between the re-entrant jet and the cavity causes periodical shedding of the cloud cavitation.

Furthermore, some cryogenic experiments have been reported for various flow configurations. Hord (1973) [6] performed experimental studies with flow visualization on a cryogenic cavitating flow around a two-dimensional symmetric thick hydrofoil by using LN_2 and LH_2. Thereafter, in order to study a high-speed chocked flow of LN_2, LOX and LCH_4 with cavitation, experiments with three nozzles of different shape were carried out by Simoneau and Hendricks (1979) [7], who made no effort to visualize the flow patterns. Several U.S. groups (1988-1994) [8-11] reported on a subsonic flow of LHe, however measurements were only for pressure or mass flow rate, not for flow visualization. There have been only a few studies to visualize cryogenic cavitation, because of difficulty in the experiments. Hori et. al. (2000) [12] performed visualized experiments on the LN_2 cavitating flow by employing the same nozzle profile as Simoneau and Hendricks. Ishii and Murakami (2003) [13] reported He I and II flows in a nozzle with flow visualization successfully.

The objective of present study has been therefore to understand the cavitation behavior around a hydrofoil in a comparative way of flow visualization between the cryogen and the ordinary fluids to elucidate the distinction for periodical shedding of cloud cavitation on the hydrofoil. The authors (2005, 2009) [14, 15] reported cavitation flow patterns on the plano-convex hydrofoil using LN_2 and water as working fluids in a cryogenic cavitation tunnel as shown in figure 1(a). Periodical shedding of cloud cavitation from the hydrofoil surface was observed in the case of the positive angle of incident *AOI*, which is defined by the angle between the approaching flow and the plane surface of the plano-convex hydrofoil (see figure 2). In the present study, experiments with emphasis on periodical shedding were performed for the cases of various channel widths and hydrofoil sizes, as well as flow velocities, in order to clarify the mechanism of periodical shedding from a hydrofoil.

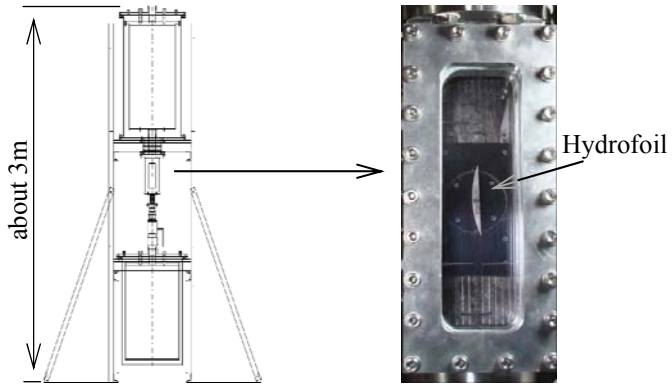

Figure 1: Cryogenic cavitation tunnel and test section

EXPERIMENTAL SETUP

In order to investigate the difference between cryogenic

Table 1: Arrangement of hydrofoils and channel widths

	W=20mm	W =30mm	W =60mm
L_C =20mm	d_{min} =8.8mm d_{max} =12.4mm d_{min}/d_{max} =0.71	d_{min} =13.8mm d_{max} =17.4mm d_{min}/d_{max} =0.79	d_{min} =28.8mm d_{max} =32.4mm d_{min}/d_{max} =0.89
L_C =60mm	–	d_{min} =11.3mm d_{max} =22.1mm d_{min}/d_{max} =0.51	d_{min} =26.3mm d_{max} =37.1mm d_{min}/d_{max} =0.71

L_C=20mm W=60mm | L_C=20mm W=30mm | L_C=20mm W=20mm | L_C=60mm W=60mm | L_C=60mm W=30mm

Figure 2: Hydrofoil and channel profiles

cavitation and ordinary fluid cavitation, liquid nitrogen as cryogen and water as ordinary fluid were employed because of easy handling and affordability. The experiments were conducted using a cryogenic cavitation tunnel of a blowdown type as shown in figure 1. This tunnel has 100L upper and lower tanks for liquid nitrogen and water. A test section, 288mm in length, 60mm in width, and 20mm in depth, with flow visualization was set between the tanks. Two sizes of plano-convex hydrofoils, which have a plane surface on one side, a convex on the other side, sharp leading and trailing edges, and thin thickness like an inducer impeller of a turbo-pump for a rocket engine, were used. Their chord lengths L_C, radii of the convex surfaces, and thicknesses were 20 and 60mm, 26 and 78mm, 2 and 6mm, respectively. The angle of their leading and trailing edges was 22.6°. In addition, the cannel width W was varied by inserting blocks in the channel. Five combinations of L_C and W were employed as shown in table 1 and figure 2. Especially the channels with L_C =W=60mm and L_C =W=20mm were similar to each other. In the experiments for various AOI ranging from −8º to 8º, periodical shedding of cloud cavitation was observed most notably at 8º (see figure 2). Therefore, in this paper, the results for AOI=8° are reported. Inlet velocity u_{in}, inlet temperature T_{in}, and inlet pressure P_{in} were varied to control cavitation number σ=$\{P_{in}-P_{sat}\}/\{\rho u_{in}^2/2\}$, where P_{sat} and ρ are saturation pressure and liquid density, respectively, for the inlet condition. u_{in} was altered by the pressure in the upper tank, which was pressurized by high-pressure gaseous nitrogen. u_{in} was evaluated by measurement of liquid level in the upper tank using a liquid level gage of a differential pressure type. T_{in} was set with an electric heater in the case of water. In the case of liquid nitrogen, heat inflow from the surroundings was balanced by evacuating the upper tank until a desired saturation temperature and pressure were achieved. This method can reduce the liquid nitrogen temperature 5K below the saturation temperature of 78K at atmospheric pressure. T_{in} and P_{in} were measured at 60mm upstream from the center of the hydrofoil. The temperature was measured by a RTD (Resistance Temperature Detector). The backpressure in the lower tank was changed by adjusting the valve opening at the outlet pipe from the lower tank to the atmosphere. It was monitored by an electronic pressure gage. In addition, there were two pressure taps on the convex surface of the hydrofoil. They were located at 3mm upstream (P_{up}) and downstream (P_{down}) from the center of the hydrofoil with L_C =20mm, and at 9mm with L_C =60mm. Flow pattern of cavitation was recorded using an ordinary digital video camera and a high-speed video camera. Their recording rates were 30 and 1000 flames per second, respectively. A trigger signal of the high-speed video camera, u_{in}, T_{in} and the other pressure signals were recorded by a data logger and PC.

RESULTS

Figure 3(a) shows a temporal change of P_{in}, P_{up}, P_{down}, T_{in} and u_{in} in the case of water, L_C =20mm, W=30mm, and P_{back}=101.3KPa as an example. In phase 1, the liquid in the upper tank was pressurized by closing the main valve between the test section and the lower tank until the pressure reached the target value. After that, in phase 2, the main valve was instantaneously opened, and the liquid flowed downward

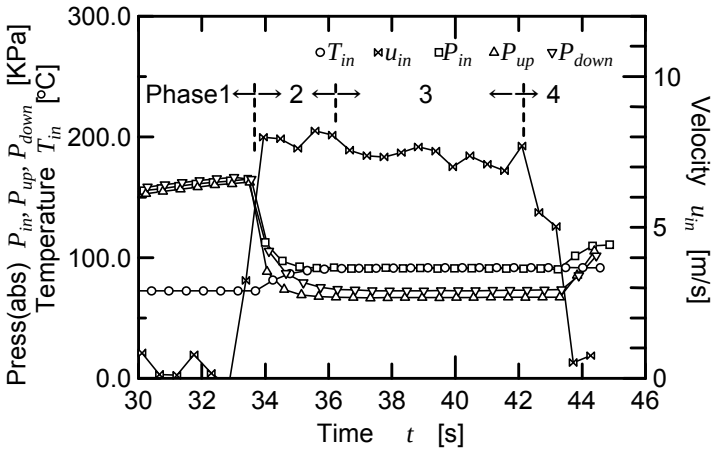

(a) Temporal change of P_{in}, P_{up}, P_{down}, T_{in} and u_{in}

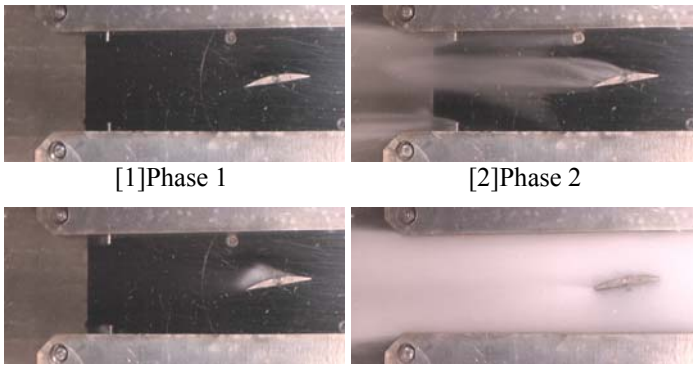

[1]Phase 1 [2]Phase 2

[3]Phase 3 [4]Phase 4

(b) Cavitation profiles

Figure 3: Timing of data acquisition
(water, L_C=20mm, W=30mm, P_{back}=101.3KPa)

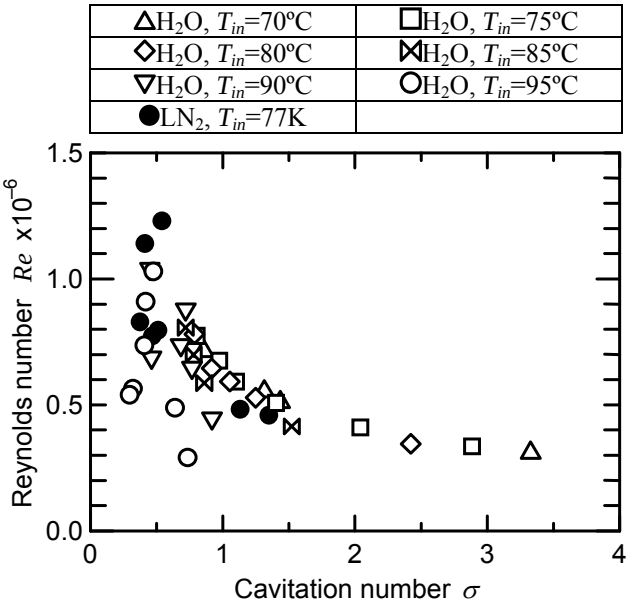

Figure 4: Characteristics of the cavitation tunnel

through the test section. Large-scale cavitation as shown in figure 3(b)[2] occurred for a few seconds due to rapid acceleration by the steep pressure gradient. Then in phase 3, steady cavitation was achieved as shown in figure 3(b)[3]. The

cavitation region was smaller than that in phase 2, and unless otherwise stated, the pictures recorded by a high-speed video camera in phase 3 were used for picking up L_{max}. After the liquid in the upper tank had almost flowed out, it switched to mist flow as shown in figure 3(b)[4] and the experiment was over.

Figure 4 shows a relationship between the Reynolds number $Re=u_{in}L_C/\nu$ and σ in the case of $L_C=W=20$mm, and $P_{back}=101.3$KPa. Experiments for a wide range of σ can be performed at small Re, whereas at large Re experiments only for a narrow range of σ can be performed due to the characteristics of the current apparatus. In other combinations of the hydrofoil and channel width, similar tendencies were observed.

Figure 5 shows a relationship between the non-dimensional cavitation length L_{max}/L_C and σ for $W=20$ and 60mm using the same foil with $L_C=20$mm. Data points at the upper limit of the ordinate ($L_{max}/L_C=5.0$) denote that the cavity region exceeds the visualization window and the real cavitation lengths were larger than $L_{max}/L_C=5.0$. In the case of $W=20$mm cavitation occurred for $\sigma\leq1.56$, however, in the case of $W=60$mm it occurred for $\sigma\leq1.21$. It is apparent that cavitation in the narrower channel easily occurs at the higher σ. The periodical shedding of cloud cavitation mainly occurs in a range of $L_{max}/L_C=1.0$ to 1.3. This result indicates that the cavitation whose L_{max} is nearly the same as L_C is especially unstable and tends to a result in periodical shedding of cloud cavitation. In the case of steady cavitation, the non-dimensional cavitation length L_{max}/L_C for $W=20$mm is larger than that for $W=60$mm. In the case of the larger hydrofoil $L_C=60$mm, the similar tendency was observed.

Figure 6 shows a relationship between L_{max}/L_C and Re. Figures 6(a) and (b) show results of $L_C=20$mm and 60mm, respectively. Data points at the upper limit of the ordinate in these figures denote that the cavity region exceeds the visualization window. In H_2O as well as LN_2, there was no cavitation at small Re. Cavitation inception occurred at a certain Re depending on W and L_C although cavitation did not occur even at high Re in some cases. L_{max}/L_C was generally getting larger with increasing Re for the same condition. Based on a comparison of figures 6(a) (b), cavitation for $L_C=20$mm

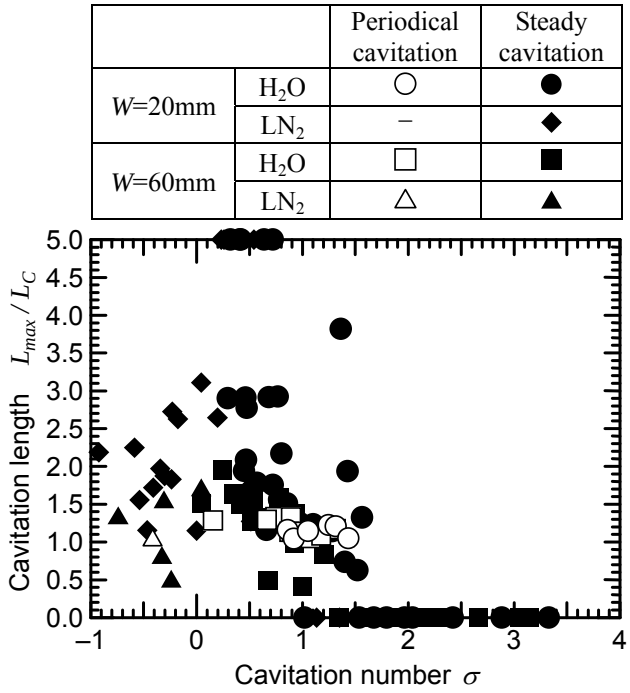

Figure 5: Cavitation length v.s. cavitation number (H_2O and LN_2, $L_C=20$mm, $P_{back}=101.3$KPa)

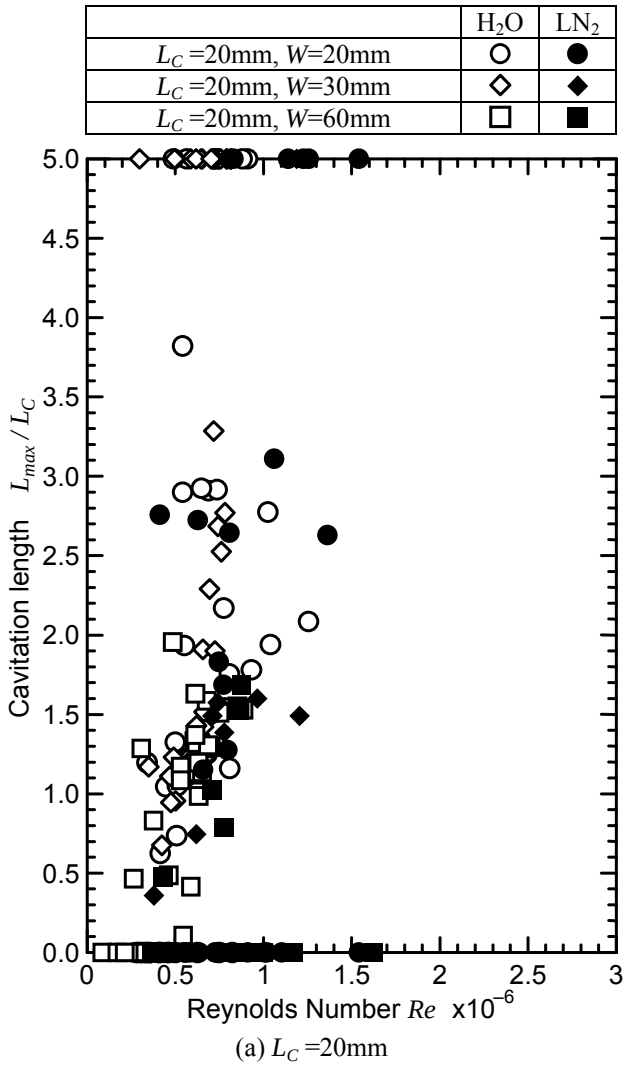

(a) $L_C=20$mm

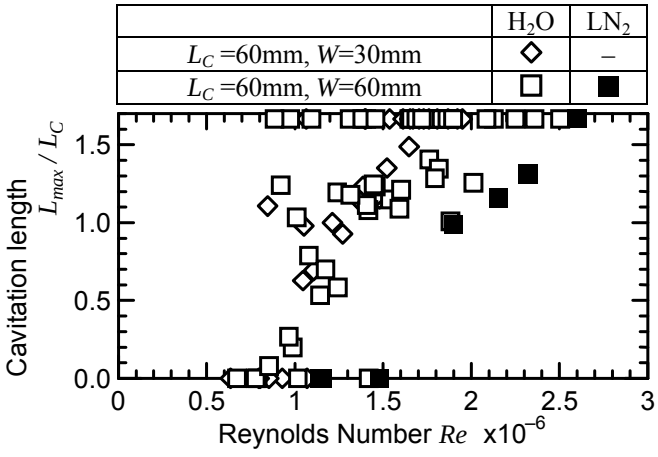

(b) $L_C=60$mm

Figure 6: Cavitation length v.s. Reynolds number (H_2O and LN_2, $P_{back}=101.3$KPa)

occurred at smaller *Re* than that for L_C=60mm. In addition, L_{max}/L_C for LN_2 was less than that for H_2O at the same *Re*.

Cavitation patterns were sorted into types A, PB, SB and C mainly based on L_{max} compared to L_C. Type X was defined as no cavitation (L_{max} =0mm), and type A as $0<L_{max}\leq L_C$. Types SB and PB are defined as $L_C<L_{max}\leq 2L_C$, of which SB means "Steady B" and PB means "Periodical B". Type C was defined as $L_{max}>2L_C$. Figure 7 shows examples of these patterns.

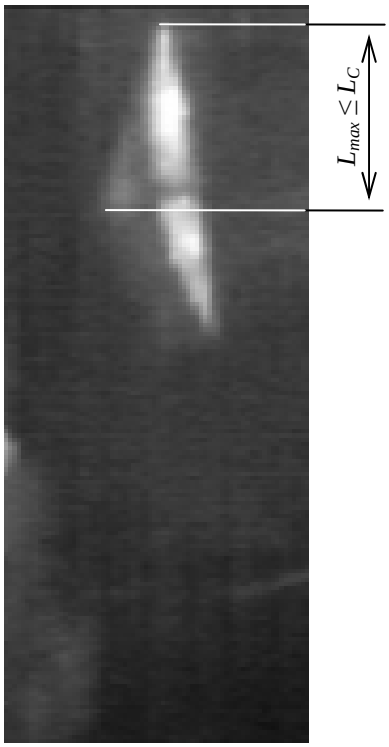

(a) Type A (*W*=30mm)
(u_{in}=4.4 m/s, σ=–0.24)

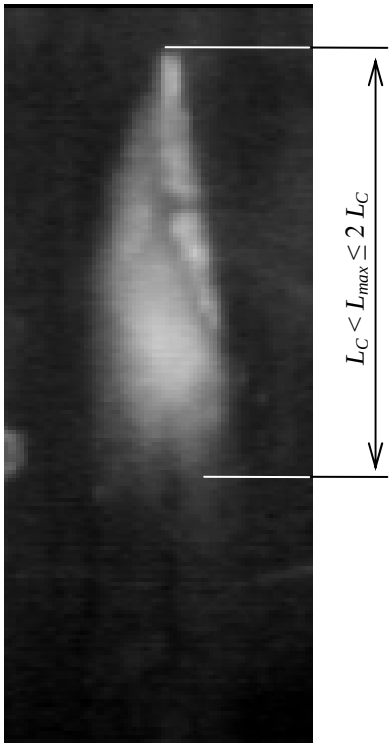

(b) Type SB (*W*=60mm)
(u_{in}=8.9m/s, σ=–0.31)

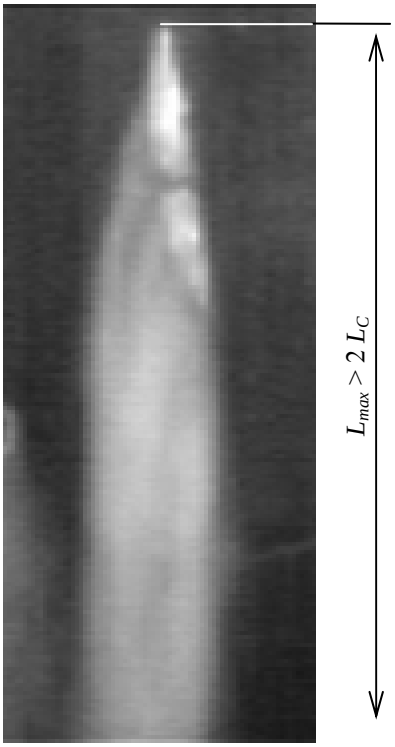

(c) Type C (*W*=30mm)
(u_{in}=12.2m/s, σ=0.20)

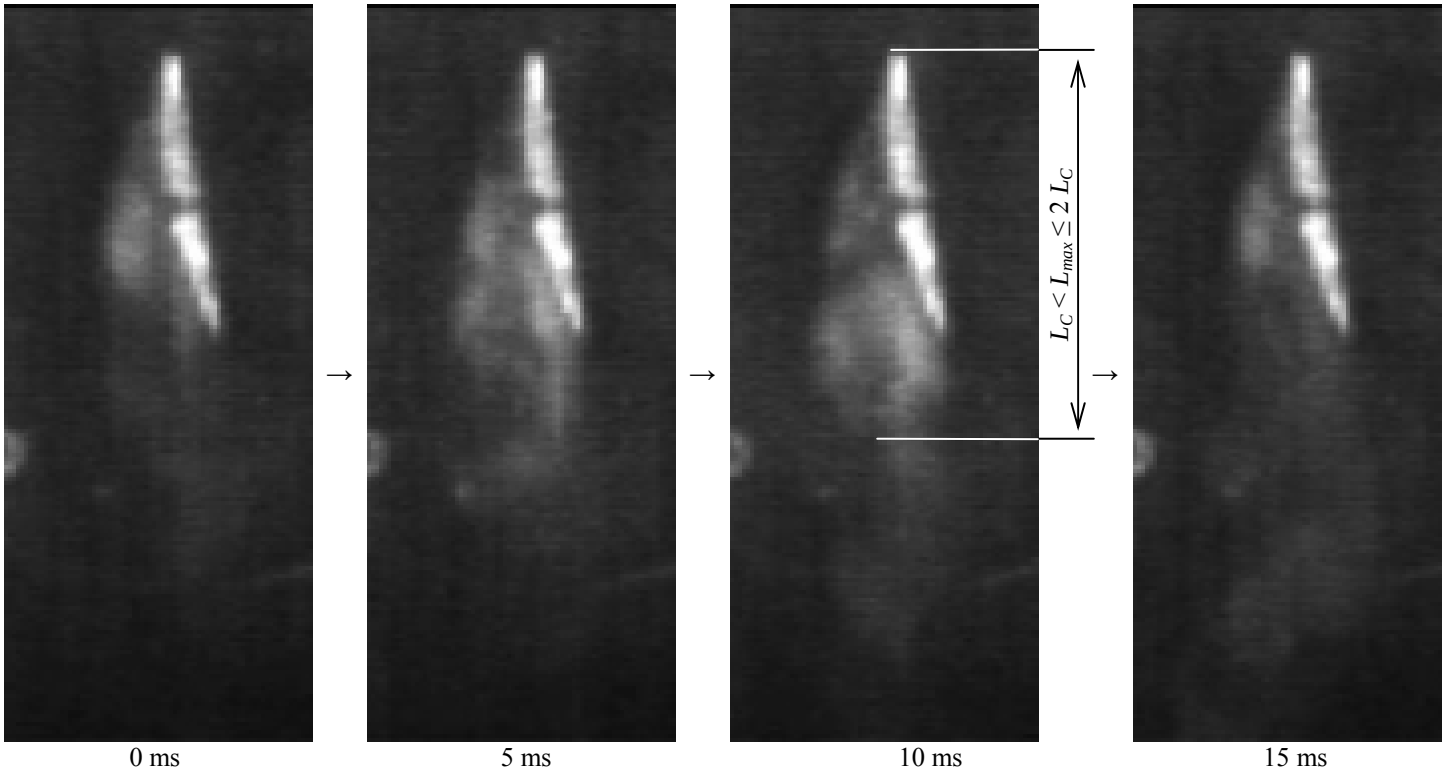

(d) Type PB (*W*=60mm, u_{in}=8.0 m/s, σ=–0.33, Shedding frequency: f_{cav}=60Hz)

Figure 7: Cavitation patterns (LN_2, L_C =20 mm)

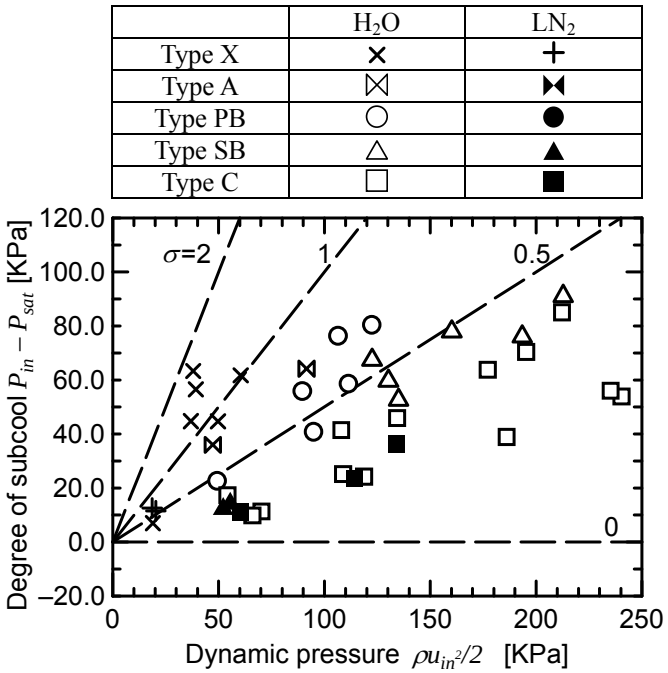

(a) L_C = 20 mm, W= 20 mm

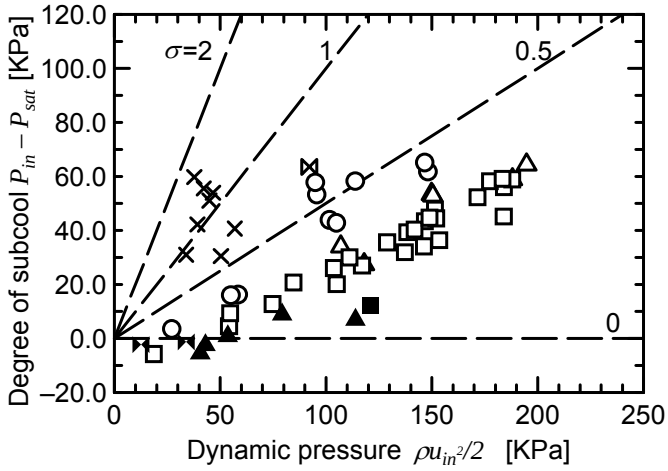

(b) L_C = 20 mm, W= 30 mm

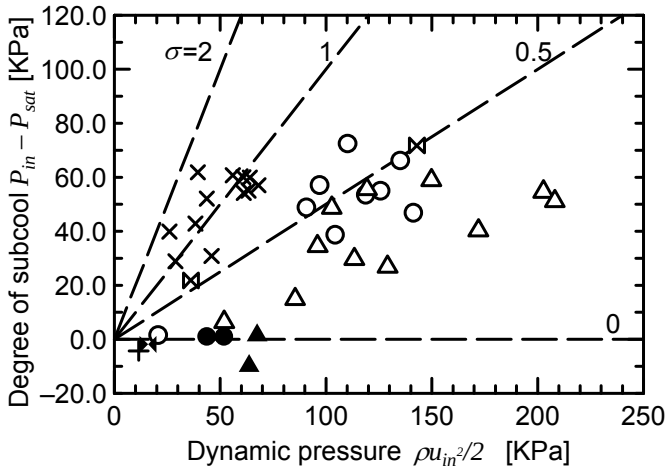

(c) L_C = 20 mm, W= 60 mm

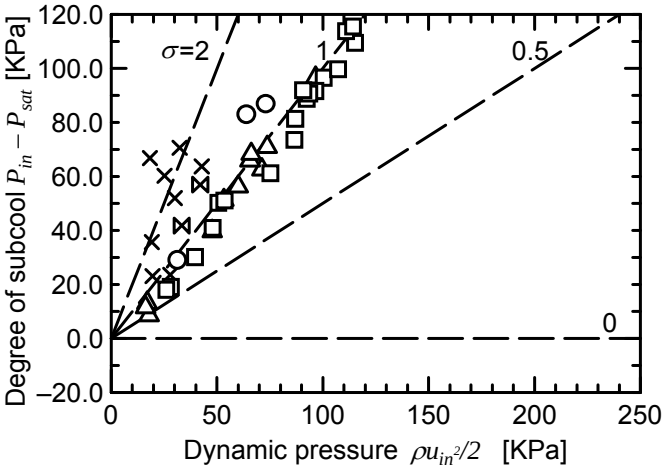

(d) L_C = 60 mm, W= 30 mm

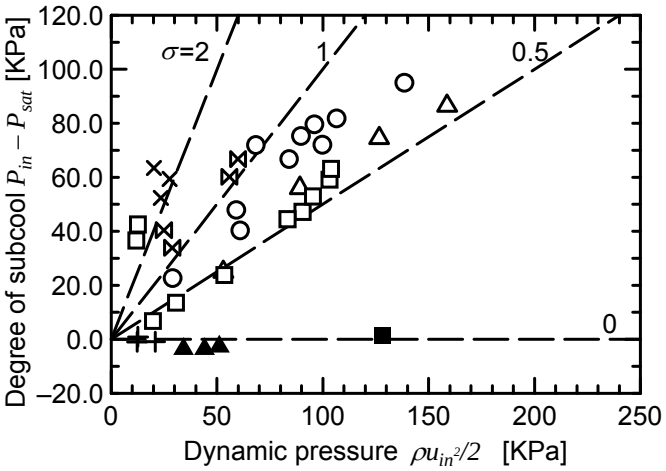

(e) L_C = 60 mm, W= 60 mm

Figure 8: Cavitation pattern Distribution (H_2O and LN_2)

Figure 7(d) shows a temporal change of the shape of the cavitation region in type PB. The cavitation formed from the leading edge of the convex suction surface, and grew along the hydrofoil surface until it fully covered the surface. Then it broke up from the trailing edge and wholly departed from the surface, and there was no cavity for a while. These processes were repeated periodically. Generally, cavitation phenomena can be classified and organized by σ. However, as shown in figure 5, various value of L_{max}/L_C were observed for the same σ, which means that the cavitation pattern cannot be determined only by σ. Therefore cavitation patterns were plotted in a diagram in which the abscissa is the dynamic pressure $\rho u_{in}^2/2$ (the denominator of σ) and the ordinate is the degree of subcooling $P_{in}-P_{sat}$ (the numerator of σ).

Figure 8 shows the cavitation pattern distribution for each channel profile. In these diagrams, contours of σ are expressed as straight lines through the origin.

First, let us focus on results of H_2O in figure 8(a). In the region above a certain σ (σ>0.9), type X (no cavitation) occurred. With decreasing σ, first type A occurred (0.8>σ>0.7) and then PB (0.8>σ>0.45). With further reducing σ, type SB occurred (~0.6>σ>0.4). Finally, type C occurred below a certain σ (σ<0.45). As shown in this figure, different types

were mixed in some regions of σ. For example, in the region of $0.8>\sigma>0.7$ (the mixed region of types A and PB), type A was observed for smaller $\rho u_{in}^2/2$, and type PB for larger $\rho u_{in}^2/2$. In the region of $\sim 0.6>\sigma>0.45$ (the mixed region of types PB and SB), type PB was observed for smaller $\rho u_{in}^2/2$, and type SB for larger $\rho u_{in}^2/2$. In the region of $0.45>\sigma>0.4$ (the mixed region of types SB and C), type SB was observed for smaller $\rho u_{in}^2/2$, and type C for larger $\rho u_{in}^2/2$. Such tendencies of transition of cavitation types were commonly observed in the results of H_2O for the other channel profiles although the locations of mixed regions of σ depend on the channel profile.

Second, let us focus on results of LN_2, in figure 8. There are only a few results for LN_2 because it was not easy to control the LN_2 temperature below the saturation value using the vacuum pump and to conduct experiments at various temperature of LN_2. However, the same tendencies as observed for the water results can be seen. In figures 8(a) and (b), type SB cavitation was observed at smaller $\rho u_{in}^2/2$, while type C was observed at larger $\rho u_{in}^2/2$ along a straight line of constant σ. In figure 8(c), type PB occurred at smaller $\rho u_{in}^2/2$, while type SB occurred at larger $\rho u_{in}^2/2$ for the same σ (nearly equals 0 in this case).

These results (types A and PB occurred at the same σ, and so did types PB and SB, and types SB and C) correspond to the fact that at given σ the longer cavitation cloud occurred at higher u_{in}, as also found in figure 6.

Figure 9(a) shows a relationship between the maximum cavitation thickness δ_{max} and σ, in the case of types SB and C, where δ_{max} denotes the maximum distance from the trailing edge of the hydrofoil to the outer edge of the cavitation region (see figure 2). For each channel, profile (combination of L_C and W) δ_{max} remains almost constant against a change of σ. Moreover, for each hydrofoil δ_{max} virtually did not vary with W. Furthermore, this was valid even when the fluid was switched from H_2O to LN_2. In other words, δ_{max} was roughly decided by the hydrofoil size ($\delta_{max}\approx$7mm for L_C=20mm, and $\delta_{max}\approx$21mm for L_C=60mm). Figure 9(b) shows cavitation profiles of L_C =60mm operating in H_2O and LN_2. It is apparent that switching the fluid from H_2O to LN_2 and changing W from 60mm to 30mm did not affect δ_{max}.

Figure 10(a) shows a relationship of σ versus the frequency of periodical shedding of cloud cavitation f_{cav}. There was no predominant tendency between σ and f_{cav}. Then, relationships of $\rho u_{in}^2/2$ versus f_{cav}, and $P_{in}-P_{sat}$ versus f_{cav} were shown in figures 10 (b) and (c), respectively. Although the data were scattered in a wide range, tendencies might be identified that for each condition. f_{cav} was low for the small values of $\rho u_{in}^2/2$ and $P_{in}-P_{sat}$, and f_{cav} was high for the large values of $\rho u_{in}^2/2$ and $P_{in}-P_{sat}$.

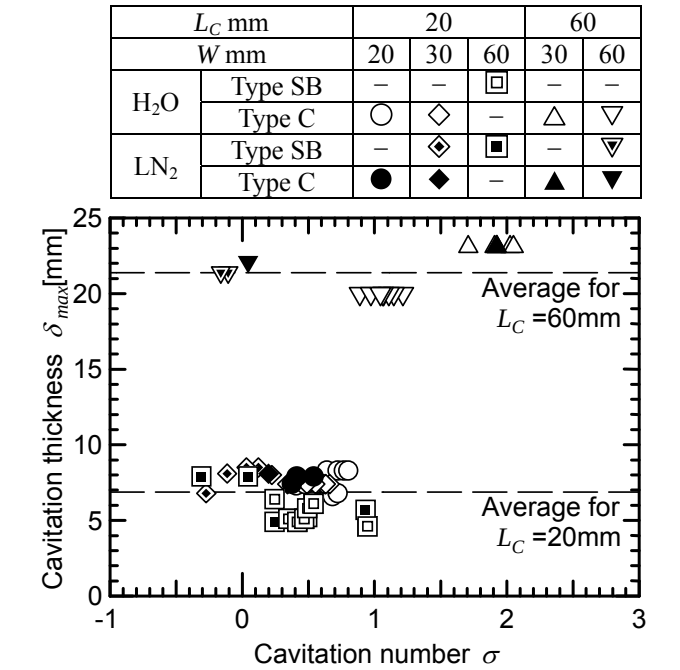

(a)Cavitation thickness v.s. cavitation number

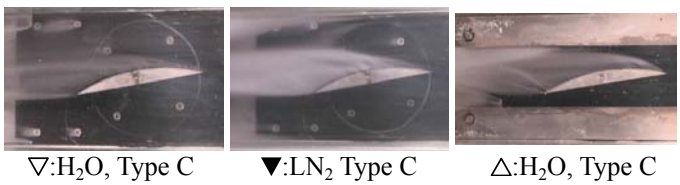

▽:H_2O, Type C W=60mm ▼:LN_2 Type C W=60mm △:H_2O, Type C W=30mm

(b)Example of cavity profile in each condition (L_C =60mm)

Figure 9: Cavitation thickness at types SB and C (H_2O and LN_2)

DISCUSSION

First, the effect of channel width on cavitation is discussed. As mentioned in relation to figure 5, when W=20mm, the cavitation inception occurred at larger σ, L_{max} was longer, and L_{max} more suddenly increased with decreasing σ than when W=60mm. The above tendencies can be explained by the blockage effect of the hydrofoil and cavitation, that is, the flow acceleration due to the blockage effect is larger for the narrower channel that promotes the onset and growth of cavitation as illustrated in figure 11. In the case of L_C =20mm, the blockage ratios of the hydrofoil are 18% and 6% for W=20mm and 60mm, respectively. Then the increase of flow velocity due to the blockage effect for liquid single-phase flow is roughly estimated as follows:

$u_{20mm}=u_{in}/(1-0.18)=1.22u_{in}$ when W=20mm

$u_{60mm}=u_{in}/(1-0.06)=1.064u_{in}$ when W=60mm

Therefore, it is confirmed that the flow acceleration is significant especially for the narrower channel. When cavitation occurs, the flow acceleration due to the blockage becomes more pronounced as illustrated in figure 11. Such a larger blockage effect for the narrower channel causes the onset of cavitation at larger σ and the rapid increase of L_{max} with the decrease of σ.

Second, the frequency of periodical shedding of cloud cavitation is discussed. A vortex of wake type like Karman vortex could cause the periodical shedding of cloud cavitation. The frequency of vortex shedding f_{vor} from a circular cylinder is given by the following empirical correlation [16].

$$f_{vor} = 0.198\frac{u_{in}}{D}\left(1-\frac{19.7}{Re_D}\right) \qquad (1)$$

where, D is the diameter of a cylinder, and Re_D is defined as $Re_D = u_{in}D/\nu$. Equation (1) was applied to the present

	H_2O	LN_2
L_C =20mm, W=20mm	○	–
L_C =20mm, W=30mm	△	–
L_C =20mm, W=60mm	◇	◆
L_C =60mm, W=30mm	⋈	–
L_C =60mm, W=60mm	□	–

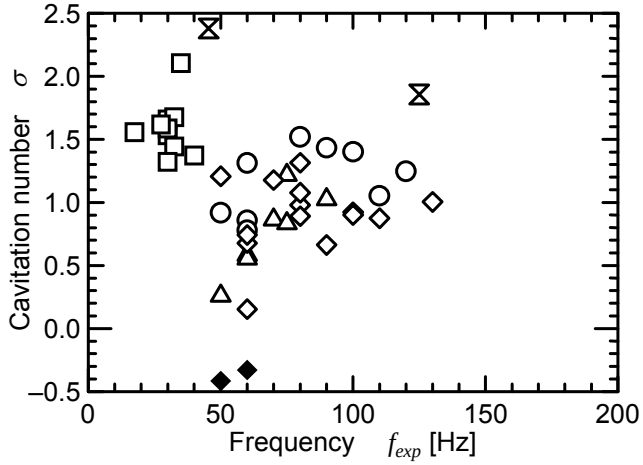

(a)Cavitation number v.s. frequency of periodical cavitation

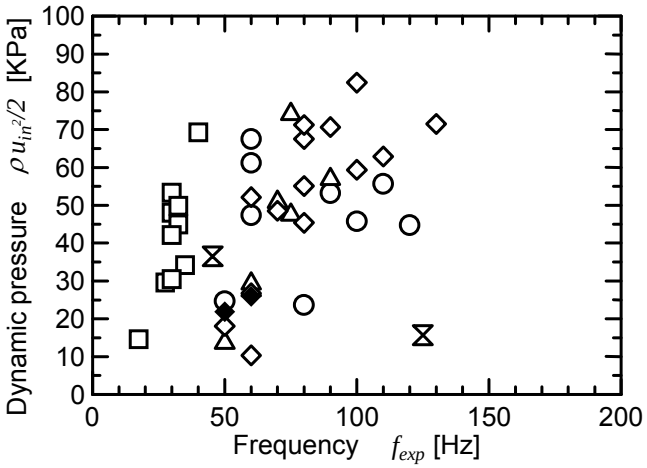

(b)Dynamic pressure v.s. frequency of periodical cavitation

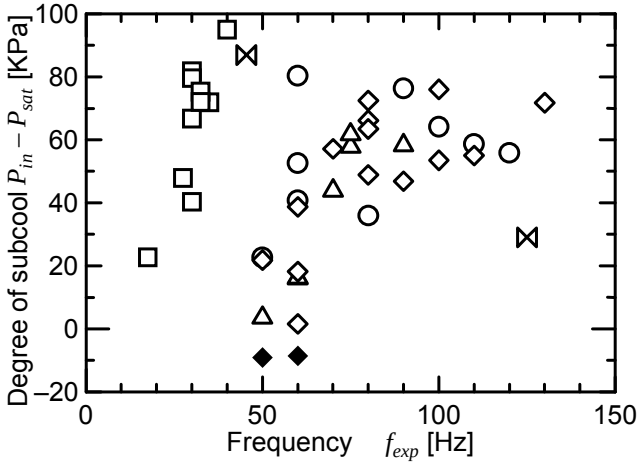

(c)Degree of subcool v.s. frequency of periodical cavitation

Figure 10: Frequency of periodical cavitation, i.e. type PB

experiment by replacing D with the maximum cavitation thickness δ_{max}, and the resulting f_{vor} is compared with f_{cav} in figure 12. f_{vor} is much higher than f_{cav} of the periodical shedding of cloud cavitation. Therefore the periodical shedding of cloud cavitation seems to be controlled by another mechanism rather than the vortex shedding of the wake.

A reverse liquid flow on the hydrofoil could also cause the periodical shedding of cloud cavitation. It is well known that periodical shedding of cloud cavitation in partial cavitation is caused by a reverse liquid flow called as a re-entrant jet [5]. In conventional cloud cavitations, the length of cavity is shorter than the hydrofoil chord length, and the liquid jet emerges at the reattachment point of liquid flow on the hydrofoil. However, the reverse liquid flow in this experiment is not the conventional re-entrant jet because the periodical shedding of cloud cavitation occurs even when the cavitation fully covers the hydrofoil surface. Figure 13 shows a temporal change of cavitation profiles in the case of type PB. Cavitation forms from the leading part of the hydrofoil and gradually grows up along the hydrofoil (0–25msec). When the cavitation reaches a certain size (26msec), the rear part of the cavitation begins to detach from the hydrofoil surface due to a reverse liquid flow between the hydrofoil surface and the cavitation region. The rear part of the cavitation continues to grow with the reverse liquid flow beneath the cavitation until the cavitation fully

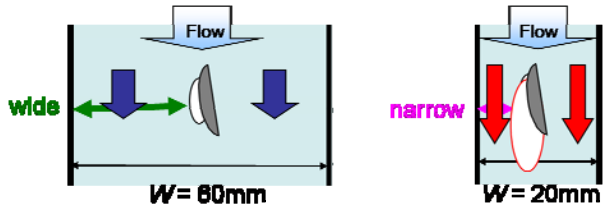

Figure 11: Schematic figures of flow velocity around the hydrofoil for wide and narrow channels

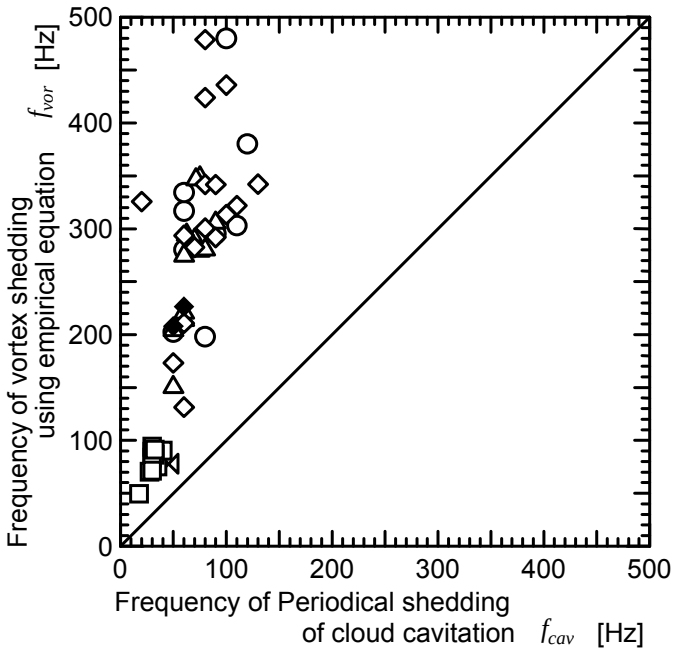

Figure 12: Comparison of frequencies between Experimental and Theoretical results

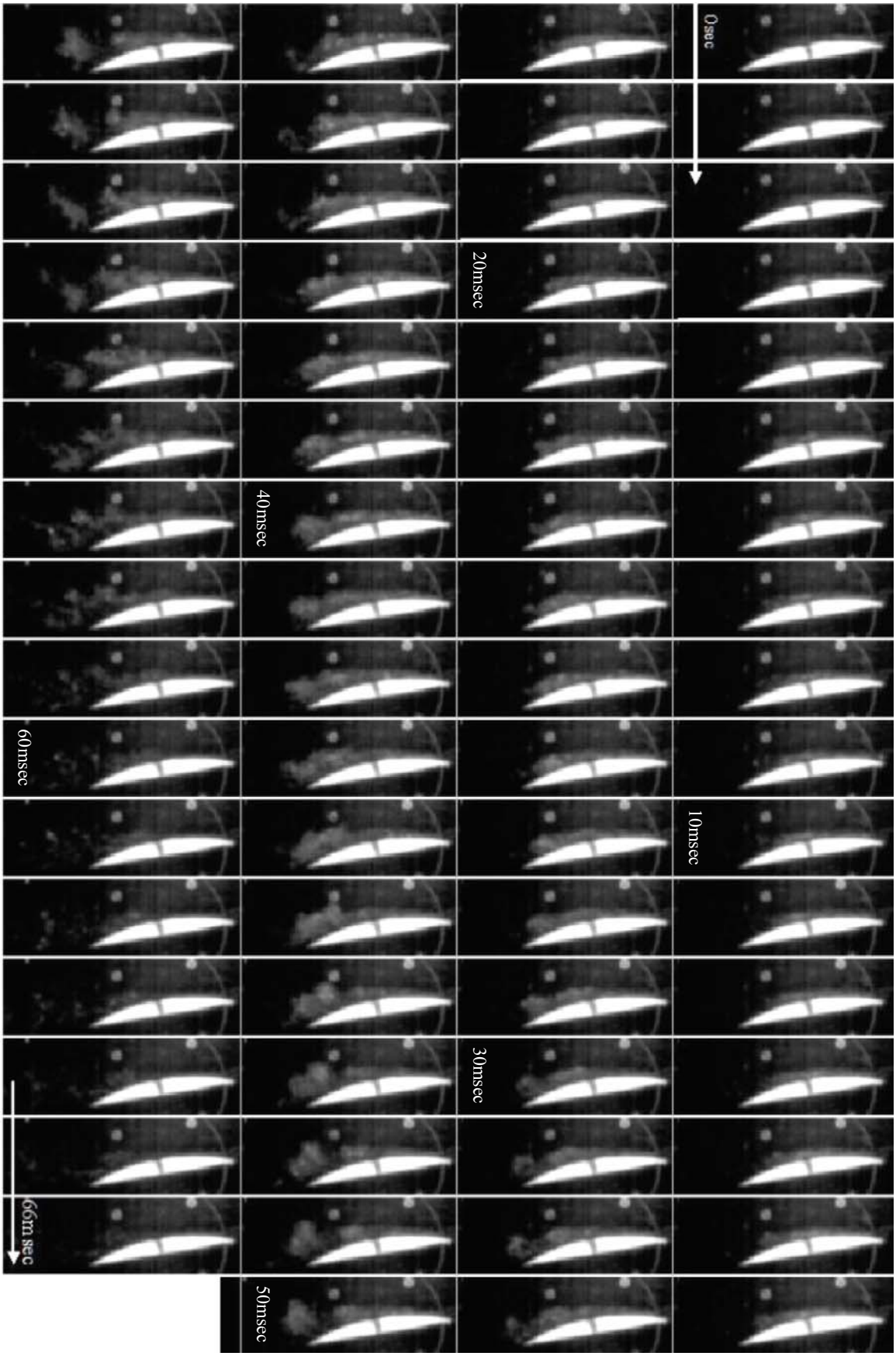

Figure 13: Temporal change of cavitation profiles (Recording speed = 1000 flames/s, Shutter speed = 1/50000s) (H_2O, L_C =60mm, W=60mm, T_{in}=95ºC, u_{in}=4.5m/s, σ=0.6)

covers the hydrofoil, and finally the rear part of the cavitation is torn off and shed (at 30msec). Although it is not clear in the still photographs, a circulating flow was observed in the rear part of the cavitation in the high-speed movie, which means that flow separation occurs in the cavitation region. The reverse liquid flow and circulation are caused by an adverse pressure gradient along the hydrofoil as indicated by P_{up} and P_{down} in figure 3. Such an interaction between the flow separation and cavitation region seems to be essential for the occurrence of periodical shedding of cloud cavitation. The growth and shedding of cavitation is repeated, and cavitation is almost completely disappears at last (at 66msec).

Based on the experimental observations, the mechanism of periodical shedding of cloud cavitation (type PB) and the flow structures of other types (A, SB and C) can be explained as illustrated in figure 14. In the case of type A, cavitation region does not reach the flow separation point, as shown in figure 14(a), which results in a stable cavitation. In the case of type PB shown in figure 14(b), cavitation reaches the flow separation region. In the separation region, the rear part of cavitation is shed by the reverse liquid flow and carried by the main liquid flow. In the case of types SB and C, thick and long cavitation covers the whole separation region as shown in Figure 14(c). Although the flow separation and circulation flow exist in the cavitation region, the shape of the cavitation region is not affected greatly by the separation region because of the large size of the cavitation. Therefore, periodical shedding of cloud cavitation (type PB) occurs when the length of cavitation region is nearly the same as the hydrofoil chord length as shown in figure 5.

CONCLUSION

A visualization study of cavitation on the convex surface of a plano-convex hydrofoil has been made for several channel widths and foil sizes using water and liquid nitrogen as the working fluid. The conclusions are summarized as follows:

(1) Cavitation patterns are sorted mainly based on the maximum cavitation length and mapped with reference to subcooling and dynamic pressure of the inlet flow. Generally, the cavitation length increases with the decrease of cavitation number. In addition, the cavitation length tends to become larger for larger inlet velocity under the same cavitation number.

(2) Periodical shedding of cloud cavitation was observed when the cavitation length was nearly the same as the hydrofoil length. Its frequency is much smaller than that estimated by an empirical equation for the vortex shedding from a bluff body. The visualization by a high-speed video revealed that a flow separation and circulating flow occur in the rear part of cavitation, and a reverse liquid flow on the hydrofoil surface tears off the cavitation resulting in the periodical shedding. For longer and thicker cavitation the circulation region exists stably in the cavitation, and periodic shedding does not occur.

(3) The cavitation number at the onset of cavitation increases with the decrease of channel width due to the blockage effect. In addition, the maximum length of cavitation region increases more rapidly with the decrease of cavitation number for the narrower channel.

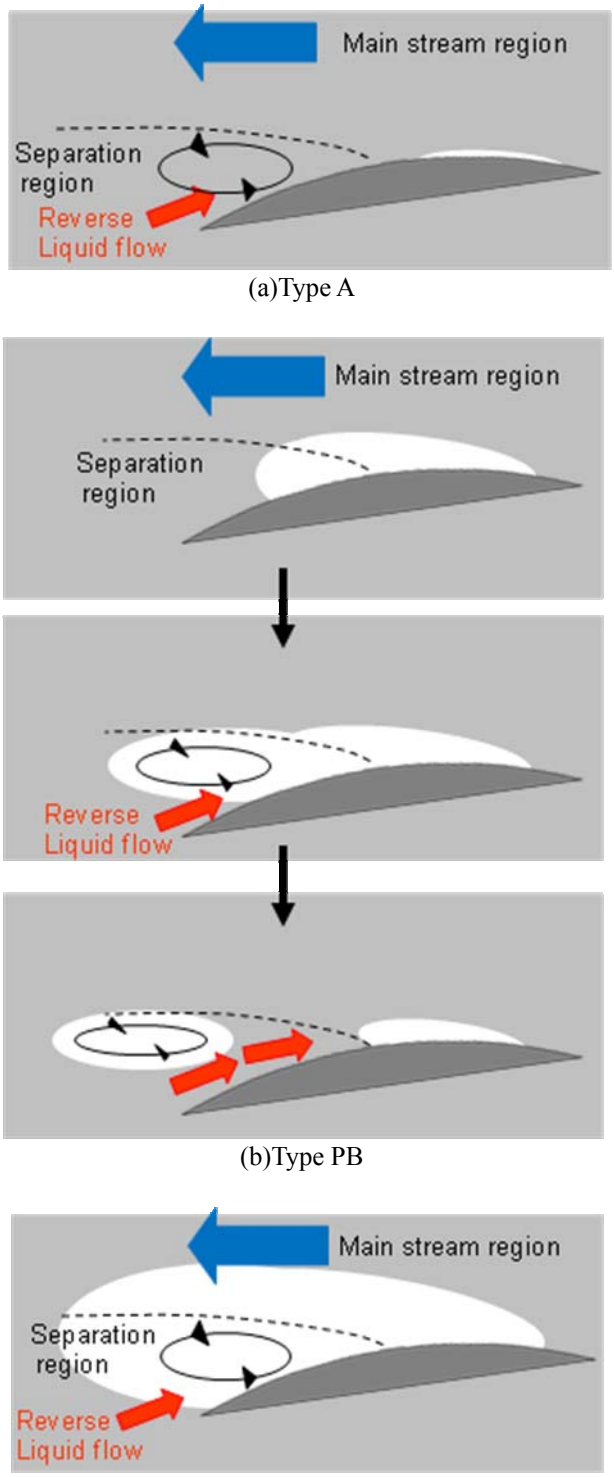

(a)Type A

(b)Type PB

(c)Types SB and C

Figure 14: Schematic figures of interaction between the cavity and the separation region

(4) The maximum cavitation thickness depends solely on the hydrofoil size for sufficiently long, thick and stable cavitation compared to the separation region, and it is independent of other experimental conditions.

ACKNOWLEDGMENTS

This work was supported by KAKENHI (14750720). The authors would like to thank Professor Toshio Nagashima at University of Tokyo for his advice and guidance.

NOMENCLATURE

A	a type of cavitation region, $L_{max} \leq L_C$
AOI	angle of the incidence between the approaching flow and the hydrofoil plane surface
B	a type of cavitation region, $L_C \leq L_{max} \leq 2\ L_C$
C	a type of cavitation region, $L_{max} \geq 2\ L_C$
d	distance
D	diameter of circular cylinder
f_{cav}	frequency of periodical shedding of cloud cavitation
f_{vor}	frequency of vortex shedding calculated by empirical equation based on the Strouhal number
H_2O	water
L	cavity length
L_C	chord length of the hydrofoil
LCH_4	liquid methane
LH_2	liquid hydrogen
LHe	liquid helium
LN_2	liquid nitrogen
LOX	liquid oxygen
P	pressure
P_{back}	pressure at the lower tank
P_{down}	pressure on the hydrofoil at 0.15 L_C downstream from the center of the hydrofoil
P_{up}	pressure on the hydrofoil at 0.15 L_C upstream from the center of the hydrofoil
Re	Reynolds number with respect to L_C
Re_δ	Reynolds number with respect to δ
St	Strouhal number
T	temperature
t	time
u	velocity
W	width

Greek characters

Δ	difference
δ	cavitation thickness
ρ	density
ν	kinetic viscosity

Subscripts

in	value at the inlet
max	value at maximum
min	value at minimum
sat	saturation value

REFERENCES

[1] Wade, R. B. and Acosta, A. J. 1966, "Experimental observation on the flow past a plano-convex hydrofoil", *Trans. ASME, J. of Basic Engineering*, 87, 273-283

[2] Le, Q., Franc, J. P. and Michel, J. M. 1993, "Partial cavities: Global behaviour and mean pressure distribution", *Trans. ASME, J. of Fluid Engineering*, 115, 243-248

[3] Kjeldsen, M., Arndt, R. E. A. and Effertz M. 1999, "Investigation of unsteady cavitation phenomena", *FEDSM*, 99-6777

[4] Franc, J. P. 2001, "Partial cavity instabilities and re-entrant jet", CAV2001, lecture. 002

[5] Callenaere, M., Franc, J. P., Michel, J. M., Riondet, M. 2001, "The cavitation instability by the development of a re-entrant jet", *J. of Fluid Mechanics*, 444, 223-256

[6] Hord, J. 1973 "Cavitation in Liquid Cryogens II – Hydrofoil", *NASA CR*, 2156

[7] Simoneau, R. J., Hendricks, R. C 1979, "Two-phase choked flow of cryogenic fluids in converging-diverging nozzle", *NASA TP*, 1484

[8] Ludtk, P. R., Daney, D. E 1988, "Cavitation characteristics of a small centrifugal pump in He I and He II", *Cryogenics*, 28, 96-100

[9] Walstrom, P. L., Weisend II, J. G, Maddocks, J. R., Van Sciver, S. W. 1988, "Turbulent flow pressure drop in various He II transfer system components", *Cryogenics*, 28, 101-109

[10] Daney, D. E. 1988, "Cavitation in flowing superfluid helium", *Cryogenics*, 28, 132-136

[11] Pettersen, M. S., Naud, C., Baliba, S., Maris, H. J. 1994, "Experimental observations of cavitation in superfluid helium-4", *Physica B*, 194-196, 575-576

[12] Hori, S., Ito, Y., Yamaguchi, K. 2000, "Observation of Cavitation Bubbles in Cryogenic 2D Nozzle Flows", *Proc. of 40th Aerospace Propulsion Conference*, 169-174, in Japanese

[13] Ishii, T., Murakami, M 2003, "Comparison of cavitating flows in He I and He II", *Cryogenics*, 43, 507-514

[14] Ito, Y., Sawasaki, K., Tani, N., Nagasaki, T., Nagashima, T. 2005, "A Blowdown Cryogenic Cavitation Tunnel and CFD Treatment for Flow Visualization around a Foil", *Journal of Thermal Science*, 14, No.4, 346-351

[15] Ito, Y., Seto, K., N., Nagasaki, T. 2009, "Periodical shedding of cloud cavitation from a single hydrofoil in high-speed cryogenic channel flow", *Journal of Thermal Science*, 18, No. 1, 58-64

[16] Massey B. 1998, *Mechanics of fluids 7th ed.*, Cheltenham : Stanley Thornes, London, UK